

JIAQING TANG<sup>1</sup>, JIE LI<sup>1</sup>, KUN LIU<sup>1\*</sup>

## EFFECT OF Ti ON MICROSTRUCTURE AND MECHANICAL PROPERTIES OF VERTICAL EGW WELDED JOINT OF 12MnNiVR STEEL

Ti-containing and Ti-free 12MnNiVR steels were welded separately by vertical EGW welding with a heat input of 100 kJ/cm. The microstructure, precipitates and inclusions of the welded joints were studied by means of optical microscope, scanning electron microscope and energy dispersive spectrometer, and the mechanical properties of the welded joints such as tensile strength, bending, and impact were tested. Results indicate that microstructure of Ti-free steel (TFS) weld metal is mainly coarse acicular and massive proeutectoid ferrite, coarse acicular ferrite Widmanstätten structure and granular bainite. The microstructure of Ti-containing steel (TCS) weld metal is mainly granular bainite and acicular ferrite. Ti has little effect on the tensile and flexural properties of welded joints, but it can improve the impact toughness of welded joints, from 101.6 J to 176.4 J at the center of weld, from 43.6 J to 80.1 J at the fusion line, from 61.5 J to 163.1 J at the fusion line + 2 mm, increasing by 73.6%, 83.7%, 165.2%, and the content of Ni and Ti in the dimples of impact fracture surface is high.

**Keywords:** 12MnNiVR steel; vertical EGW; microstructure; tensile strength

### 1. Introduction

12MnNiVR steel has the advantages of high strength, good impact toughness and good weldability [1-3]. It is widely used in the field of manufacturing large and super large oil storage tanks. The construction of oil storage tanks has high requirements on the quality of welded joints. Therefore, the research on the microstructure and properties of 12MnNiVR steel joints is of great significance for the welding and manufacturing of petroleum storage tanks [4]. In actual production, vertical electrogas welding (EGW) has become the main welding method for 12MnNiVR steel for storage tanks due to its advantages of high production efficiency, low welding cost and easy operation [5-9]. Under the action of welding thermal cycle, the grains in the heat-affected zone (HAZ) of the welded joint become coarser and HAZ becomes the weakest part of the welded joint, so fractures often occur in the heat-affected zone.

In the production of low-alloy high-strength steel, adding minor alloying elements can help generate fine and dispersed the second phase precipitation in the welded joint, which would effectively prevent the growth of austenite grains and improve the performance of the joint, especially the coarse-grained HAZ. The content of Ti in steel has significant effect the formation

of inclusions and precipitates [10-16]. The influence of Ti on microstructure and mechanical properties in large heat input welding of high strength low alloy steels is investigated [17]. It was indicated that a moderate amount of Ti is still effective for grain refinement even under larger heat input and a large amount of acicular ferrite (AF) is formed in the weld metal when Ti content is within 0.028%-0.038%. With increasing Ti content, proeutectoid ferrite in the weld metal decreases, whereas bainite and M-A constituent increase. Wang et al. [18] found that single or multiple AF grains were nucleated on complex inclusions by forming Mn-depleted zones, where Mn spontaneously diffused into Ti oxide inclusions due to the cation vacancies. The bainite nucleated on austenite grain boundary and then assisted the pre-formed AF to partition the austenite grain into small and separate regions.

TCS and TFS were welded separately by vertical EGW welding with a heat input of 100 kJ/cm in the present work. The microstructure, precipitates and inclusions of the welded joints were studied by means of optical microscope, scanning electron microscope and energy dispersive spectrometer, and the mechanical properties of the welded joints such as tensile strength, bending, and impact were tested. However, in the welding condition of high heat input, the heat-affected zone

<sup>1</sup> JIANGSU UNIVERSITY OF SCIENCE AND TECHNOLOGY, SCHOOL OF MATERIALS SCIENCE AND ENGINEERING, ZHENJIANG, 212100, CHINA

\* Corresponding author: [liu\\_kun@163.com](mailto:liu_kun@163.com)



TABLE 1

Chemical composition of steels (wt.%)

Steels	Elements												
	C	Mn	Si	P	S	Al	Cr	Ni	Mo	V	Ti	N	Fe
Non-containing Ti	0.1	1.46	0.218	0.006	0.002	0.023	0.029	0.25	0.104	0.039	—	0.003	Bal.
Containing Ti	0.095	1.46	0.218	0.009	0.001	0.026	0.023	0.24	0.105	0.042	0.02	0.003	Bal.

(HAZ) near the fusion line remains at elevated temperatures for an extended duration, resulting in a slow cooling rate. At these high temperatures, there is rapid growth of austenite grains within the HAZ, which can potentially transform into coarse grain boundaries and adversely affect microstructures such as eutectoid ferrite, Widmanstatten structure, side lath ferrite, and granular bainite that ultimately compromise the toughness of the HAZ.

2. Materials and experimental procedures

In order to investigate the effect of Ti on the microstructure and properties of welded joints, two series of 12MnNiVR steels were designed by containing Ti and non-containing Ti. The dimensions of steels used in this work was 500 mm × 200 mm × 21.5 mm. The chemical composition of steels was listed in TABLE 1. DW-S1LG filler wire was selected with diameter of 1.6 mm and the chemical composition of wire was listed in TABLE 2.

TABLE 2

Chemical composition of filler wire (wt.%)

C	Si	Mn	P	S	Ni	Mo	Fe
0.05	0.25	1.60	0.009	0.007	1.40	0.13	Bal.

Vertical electrogas welding methods was adopted in the present work to weld 21.5 mm thick plates. The selection of welding speed in gas-electric vertical welding process is closely related to the groove size. The welding process parameters of gas-electric vertical welding were listed in TABLE 3, and the schematic diagram of groove is shown in Fig. 1. The surface of

the test plate was grinded and cleaned before welding to remove rust, oil stain and other sundries.

TABLE 3

Welding process parameters

Heat input /(kJ·cm <sup>-1</sup> )	Current/A	Voltage/V	Welding speed /(cm·min <sup>-1</sup> )
100~120	360~380	36~38	8.3

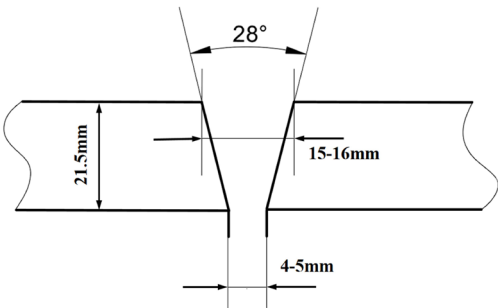


Fig. 1. Schematic diagram of groove

Penetrant testing (PT) was performed on the test plate 24 hours after welding. The color of penetrant liquid used for testing is red, which can be observed under normal light. Once red marks are found near the welded joint, the defects of the welded joint can be inferred. From Fig. 2, it can be seen that there is no red mark on the joints so no defects such as pores and cracks can be found.

After welding, the joints were cut to prepare the sample for investigating the microstructure according to the GB/T 13298-2015 standard. The samples were ground by 150-2000

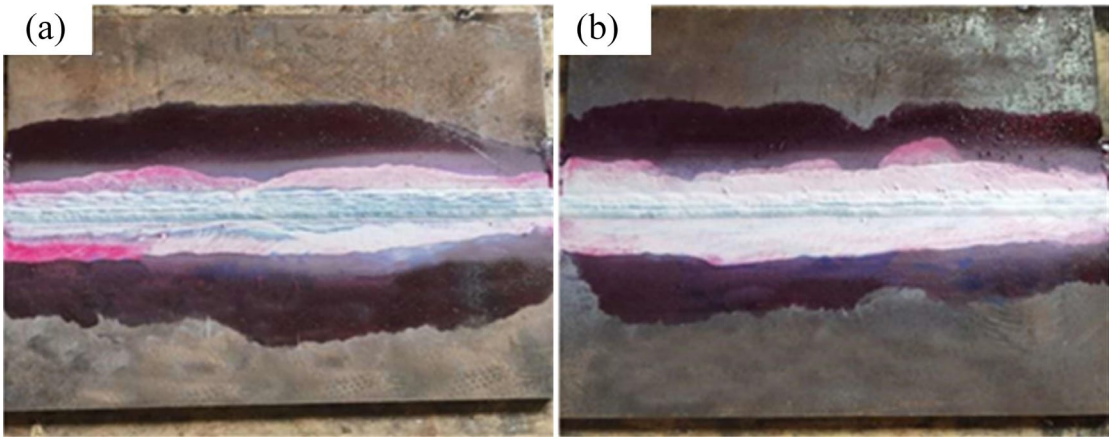


Fig. 2. Penetrant testing results of weld: (a) TCS weld, (b) TFS weld

mesh sandpaper and then were polished. The solution of 4% nitric acid with alcohol was used for etching. The metallographic samples were observed by using the ZEISS Axio Oberver A3m inverted metallographic microscope. The microstructure, precipitated phases, inclusions and morphology of impact fractures were observed by ZEISS Merlin Compact cold-field emission scanning electron microscopy and the parameters of SEM-EDX analysis in our work are as follows: accelerating voltage 15 kV and the time of map collecting 3 min.

The mechanical properties of joints were also investigated. Three samples were prepared for testing each mechanical property and the average value was calculated as final results. The notch of the impact specimen was opened at the center of the weld, the fusion line, and the fusion line +2 mm. Tensile and bending tests specimens were carried out by using CMT5205 electronic universal material testing machine. SANS pendulum impact testing machine was used to conduct impact testing. Microhardness of joints was tested by KB 30S FA BASIC automatic hardness tester machine.

### 3. Results and discussion

#### 3.1. Effect of Ti on microstructure of 12MnNiVR steel joint

Metallographic samples are prepared and observed. Fig. 4 shows the macroscopic morphology of joints of two kinds of steel plates after welding. No cracks or pores were found. It can be clearly seen that columnar dendrites distributed in the weld metal.

On the basis of macroscopic metallography, the microscopic metallography of weld metal of steel plates after welding is observed and analyzed. Fig. 4 shows metallographic pictures of weld metals of TCS and weld metals of TFS. There are obvious differences in the microstructure of weld metals between the two steels. It can be seen from Fig. 4(a) and 4(b) that the weld structure of TFS is full of granular bainite, proeutectoid ferrite is distributed along grain boundaries in coarse needle and block shape, and Widmanstatten structure of coarse needle ferrite grows into grain. Widmanstatten structure not only has coarse grains,

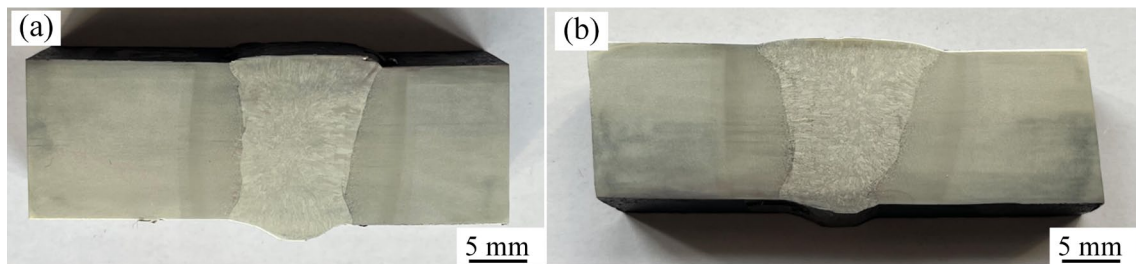


Fig. 3. Macroscopic morphology of welded joints of 12MnNiVR steel with different compositions: (a) TFS joint, (b) TCS joint

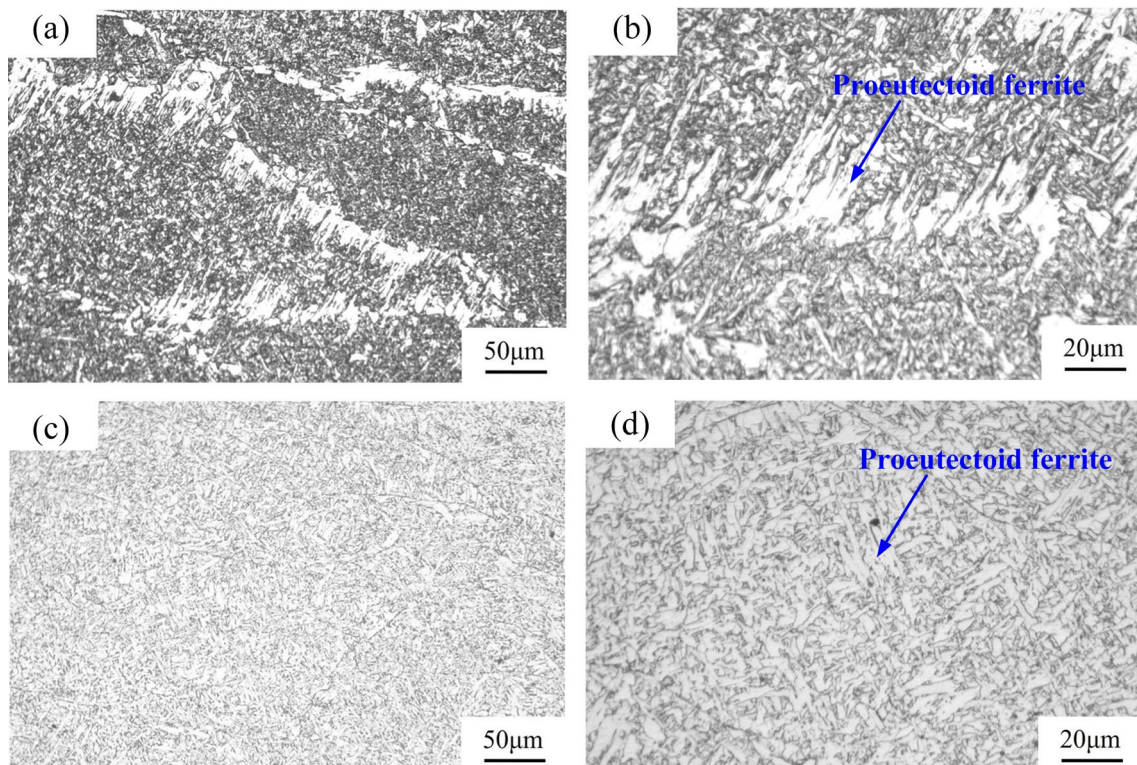


Fig. 4. Microscopic metallography of 12MnNiVR steel weld metal with different compositions: (a) TFS at low magnification, (b) TFS at high magnification, (c) TCS at low magnification, (d) (a) TCS at high magnification



but also a large number of acicular ferrite will form fragile surfaces. It is generally believed that Widmanstatten microstructure and coarse grains produced at the same time will reduce the mechanical properties of steel especially when the impact toughness and plasticity decrease most seriously, and increase the ductile-brittle transition temperature of welded joints. As shown in Fig. 4(c) and 4(d), the weld microstructure matrix of TCS is granular bainite, proeutectoid ferrite precipitated along austenite grain boundary, acicular ferrite exists in the grain, and some austenite grain boundaries can be seen. Acicular ferrite and granular bainite are fine and uniform, which is beneficial to reduce the anisotropy of weld and improve the strength and plasticity of weld.

From the above microstructure study, it can be seen that the weld metal structure of TFS is coarse acicular and massive ferrite, while the weld metal structure of TCS is granular bainite matrix, with acicular ferrite and granular bainite. The microstructure of weld metal was further observed by scanning electron microscope, and its morphology was characterized.

Fig. 5 shows the morphology of precipitated phase in weld metal of TCS and TFS. There are great differences in precipitated phases between the two kinds of steel plates after welding. From Fig. 5(a), it can be seen that the weld metal of TFS precipitates less phase inclusions, and the morphology is mainly lath bainite segregation in the grain. The distribution of M-A components is not directional, the boundary is unclear, and the morphology is mainly block and strip. The amount of M-A components is far greater than that of TCS. The more M-A components, the more serious embrittlement is, because when the residual austenite in the grain increases the carbon content, it is easy to form twin martensite. These twin martensite intermingles between bainite and ferrite lath, and produces tiny cracks at the interface between the two phases, and then propagates along the M-A component boundary. Therefore, the toughness decreases. It can be seen from Fig. 5(b) that the precipitated phase morphology of TCS weld metal is mainly segregated in grains by granular bainite and lath bainite, less segregated on grain boundaries, no continuous grain boundaries can be seen, and disordered punctate M-A components are distributed, accompanied by slender strip M-A islands. Granular bainite is composed of ferrite matrix and M-A components distributed in it [19]. There are many inclusions in weld metal, and the nucleation center of acicular ferrite is inclusions.

Partial melted zone refers to the transition zone between weld metal and base metal, which has a narrow range and the temperature is between liquidus and solidus. Under welding conditions, local melting and local non-melting parts are produced due to uneven melting at the boundary of base metal, which are irregular serrated curves on the macro level. The biggest characteristic of Partial melted zone is chemical inhomogeneity, which causes inhomogeneity in microstructure and properties, so it has great influence on the strength and toughness of welded joints. In many cases, the partial melted zone is often considered as the weakest part of joints, which is the birthplace of cracks and brittle failure.

Fig. 6 shows the microstructure of the partial melted zone of 12MnNiVR steel with different compositions, with the weld on the left side and the partial melted zone on the right side. The microstructure of the two steels in the partial melted zone shows that the metallurgical bonding is good, and the dividing line between the weld and the partial melted zone is obvious. It can be seen from Fig. 6(a) and 6(b) that the TCS has granular bainite on the left side and side lath ferrite in the partial melted zone on the right side, which is a typical Widmanstatten structure. Widmanstatten structure is a complex phase structure formed when austenite grains are coarse and cooling rate is appropriate. It is composed of proeutectoid phase mixed with lamellar pearlite in acicular form. Feathery upper bainite even appears on the upper right side of the partial melted zone in Fig. 6(b). Upper bainite is a two-phase structure, which is composed of ferrite and cementite. Discontinuous carbides are distributed between ferrite slats. Carbide particles in upper bainite are larger and strengthening effect is smaller, especially lamellar ferrite, which is easy to become a crack development channel, thus deteriorating impact toughness. However, in Fig. 6(c) and 6(d), the left side of TCS is granular bainite and acicular ferrite, and the proportion of granular bainite is much smaller than that of TFS. Fine granular bainite, side lath ferrite and acicular ferrite appear in the right partial melted zone.

The property of heat affected zone (HAZ) is determined by the microstructure of HAZ. Therefore, it is very necessary to study and analyze the structure of heat affected zone. In welded joints, the area near the weld is called coarse grain heat affected zone. In this region, the grains will grow rapidly and form coarse overheated structure. After cooling, the microstructure formed in this area is coarse, and the toughness decreases obviously. Due

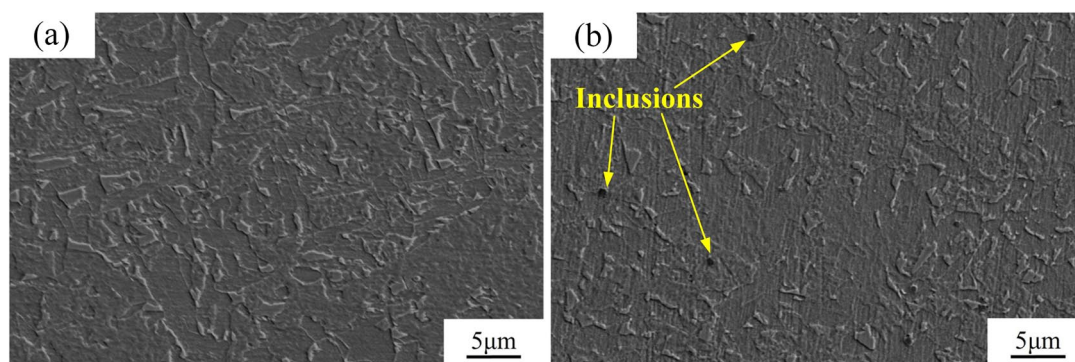


Fig. 5. SEM images of weld metal of 12MnNiVR steel welds with different compositions: (a) TFS, (b) TCS



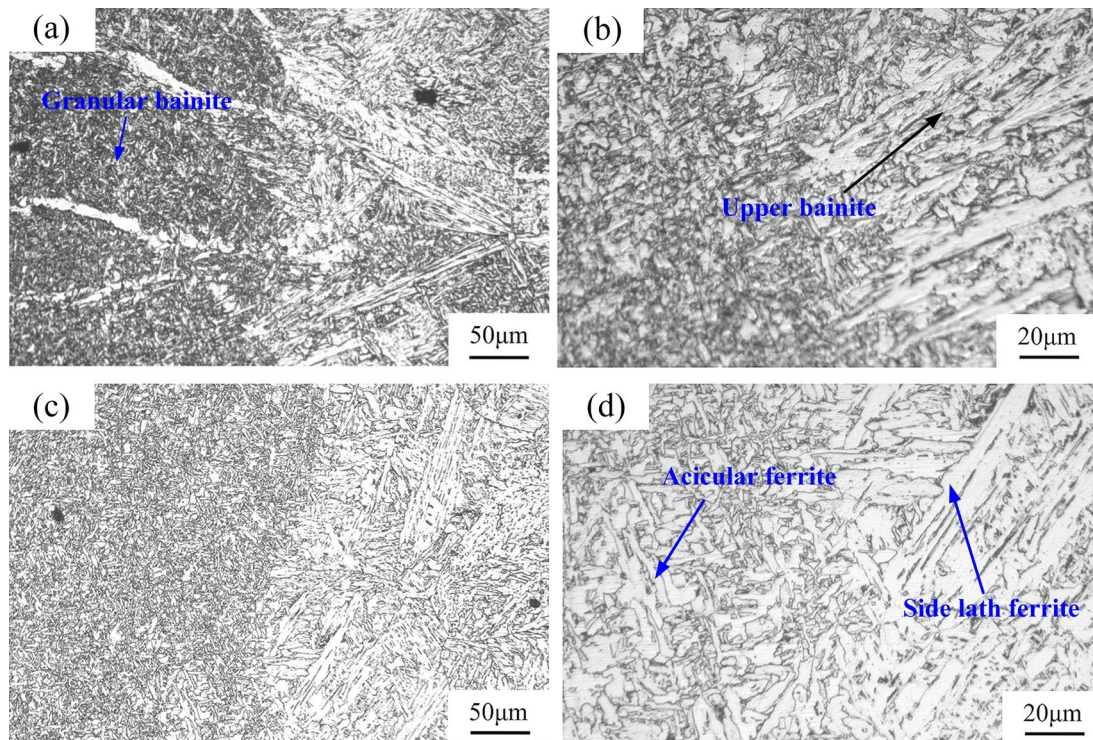


Fig. 6. Microscopic metallography of partial melted zone of 12MnNiVR steel with different compositions: (a) partial melted zone of TFS at low magnification, (b) partial melted zone of TFS at high magnification, (c) partial melted zone of TCS at low magnification, (d) partial melted zone of TCS at high magnification

to the existence of coarse grain heat affected zone, the original excellent properties of the base metal cannot be completely guaranteed. Therefore, the microstructure of coarse grain heat affected zone is mainly studied.

Fig. 7 shows the microstructure of coarse grain heat affected zone of 12MnNiVR steel. There are obvious differences in the microstructure of coarse grain heat affected zone metals between the two steels. As shown in Fig. 7(a) and 7(b), the mi-

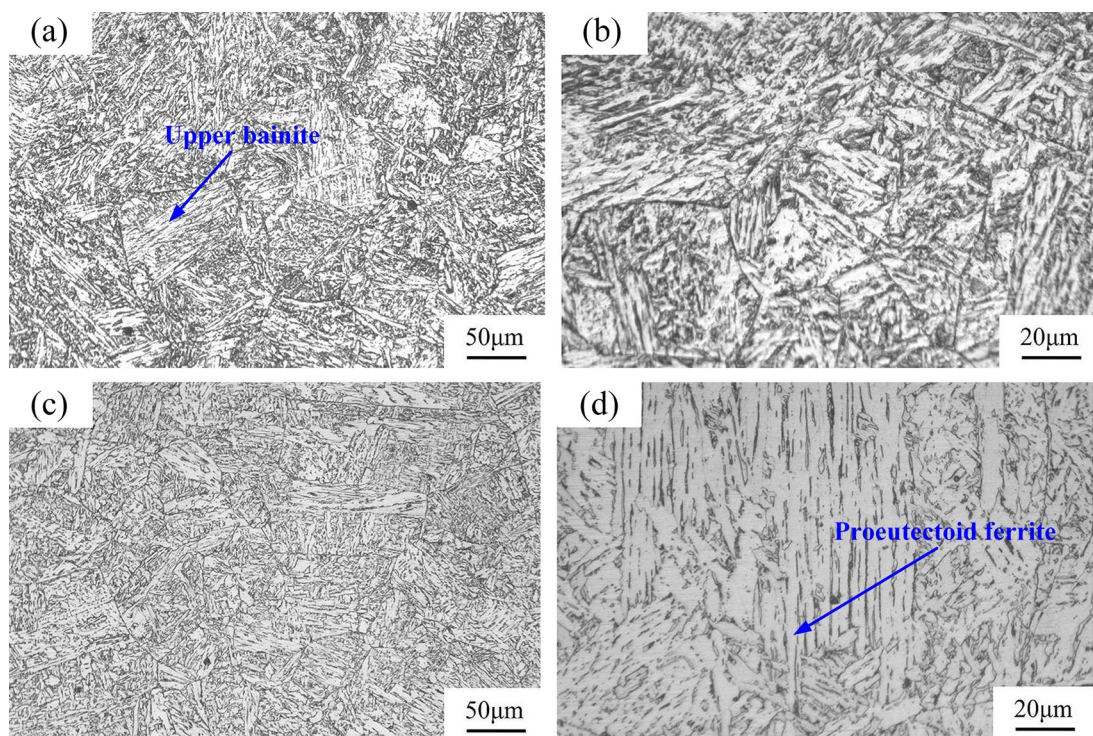


Fig. 7. Microscopic metallography of heat-affected zone of coarse grained 12MnNiVR steel with different compositions: (a) HAZ of TFS at low magnification, (b) HAZ of TFS at high magnification, (c) HAZ of TCS at low magnification, (d) HAZ of TCS at high magnification



microstructure of coarse-grained heat affected zone of TFS is based on granular bainite, with feather-like distribution of upper bainite and lath bainite, and massive ferrite precipitated along grain boundaries. From Fig. 7(c) and 7(d), it can be seen that proeutectoid ferrite is distributed at grain boundaries of coarse grains of proaustenite in the coarse-grained heat affected zone of TCS, and the proeutectoid ferrite is acicular and lath-shaped. There is not only acicular ferrite with different thicknesses, but also granular bainite and a large number of carbon-free bainite in the grains. Carbon-free bainite is also called lath ferrite, and the dislocation density of ferrite lath bundles in carbon-free bainite is high and parallel to each other, and sometimes there are strip-shaped M-A islands between lath. Usually, the formation of carbon-free bainite is produced by continuous cooling in a certain temperature range. When the temperature is high and the lath is not developed enough, some lath formation will recover, which will lead to the discontinuity of lath boundary. Carbon-free bainite plays a role in grain refinement, dislocation strengthening and subgrain strengthening on the strength and toughness of joints [20].

From the above analysis on microstructure, it can be seen that the coarse-grained HAZ of TFS is characterized by side lath ferrite and upper bainite, while that of TCS is characterized by lath bainite, acicular ferrite and massive ferrite.

Fig. 8 shows the morphology of precipitated phases in coarse-grained heat affected zone of TFS and TCS. As can be seen from Fig. 8(a), granular bainite is obvious in the coarse-grained heat affected zone of TFS. Granular bainite is not only coarse, but also exists in bundles. M-A components in lath, block or rod shape are gradually distributed at the interface between bainite bundles or bainite bundles, which can be used as crack source and induce crack generation during impact test [21]. However, in Fig. 8(b), it can be seen that the morphology of metal precipitates in the coarse-grained heat affected zone of

TCS is mainly based on granular bainite, and no continuous grain boundary can be seen. Most granular bainite is uniformly distributed in the grain in blocks perpendicular to the welding direction, and a small amount of M-A components exist.

Based on the study of precipitated phase in coarse-crystal heat affected zone, the inclusion in coarse-crystal heat affected zone is further studied. In order to identify the type of inclusions, EDS analysis of precipitated phase in coarse-grained heat affected zone was carried out. Fig. 9 shows EDS characterization of precipitated phase in coarse-grained heat affected zone of TFS, and the results of energy spectrum analysis are shown in TABLE 4.

The results of energy spectrum analysis show that the main elements of precipitated phase in coarse grained heat affected zone of TCS are C, N, Ti and Si, and the highest content of Ti is 65.33%. It can be seen from the inclusion morphology of coarse grain heat affected zone of TCS in Fig. 10 that a large square precipitated phase is formed in bainite lath. Combined with the corresponding energy spectrum analysis and the interface scanning diagram in Fig. 10, it is speculated that the precipitated phase may be TiN, Ti can combine with N element, and TiN can form a stable second phase precipitation at high temperature. These dispersed TiN can effectively hinder the growth of austenite grains and increase the nucleation density of acicular ferrite in grains.

Ti and N in coarse-grained heat affected zone will react as follows and become precipitated phases.



$$G^\circ = -308739 + 118.82T \text{ (J/mol)} \quad (2)$$

where:  $\Delta G^\circ$  is the change of standard free energy of reaction, and  $T$  is the standard temperature.

In the process of high heat input welding, TiN in coarse grain heat affected zone will be dissolved because of higher temperature. The coarsening of TiN is affected by Ti content

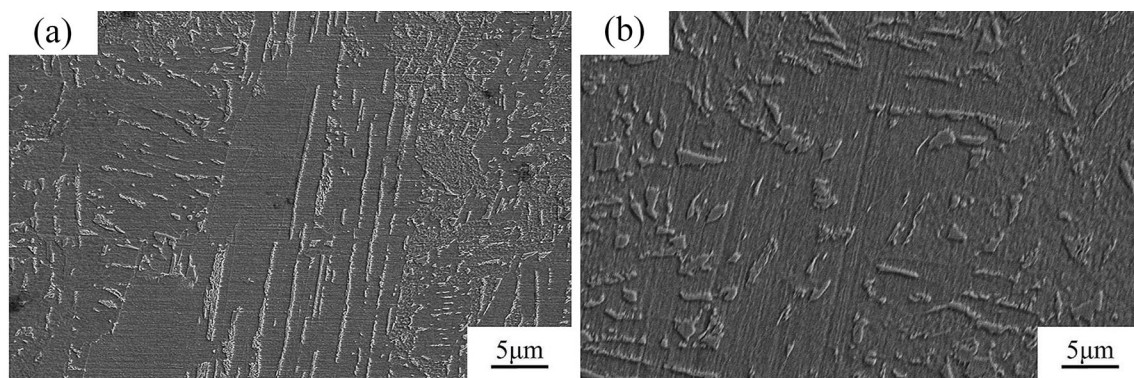


Fig. 8. SEM images of coarse-grain HAZ of 12MnNiVR steel with different compositions: (a) coarse-grain HAZ of TFS, (b) coarse-grain HAZ of TCS

TABLE 4

EDS analysis of precipitated phase (wt.%)

Precipitated phase	C	N	Ti	Al	Si	P	S	Mn	Fe	Ni	Mo
A	13.4	0.3	—	7.0	5.0	0.3	4.4	38.5	29.3	—	1.9
B	7.	24.2	65.3	—	—	—	—	0.3	2.8	0.1	0.3

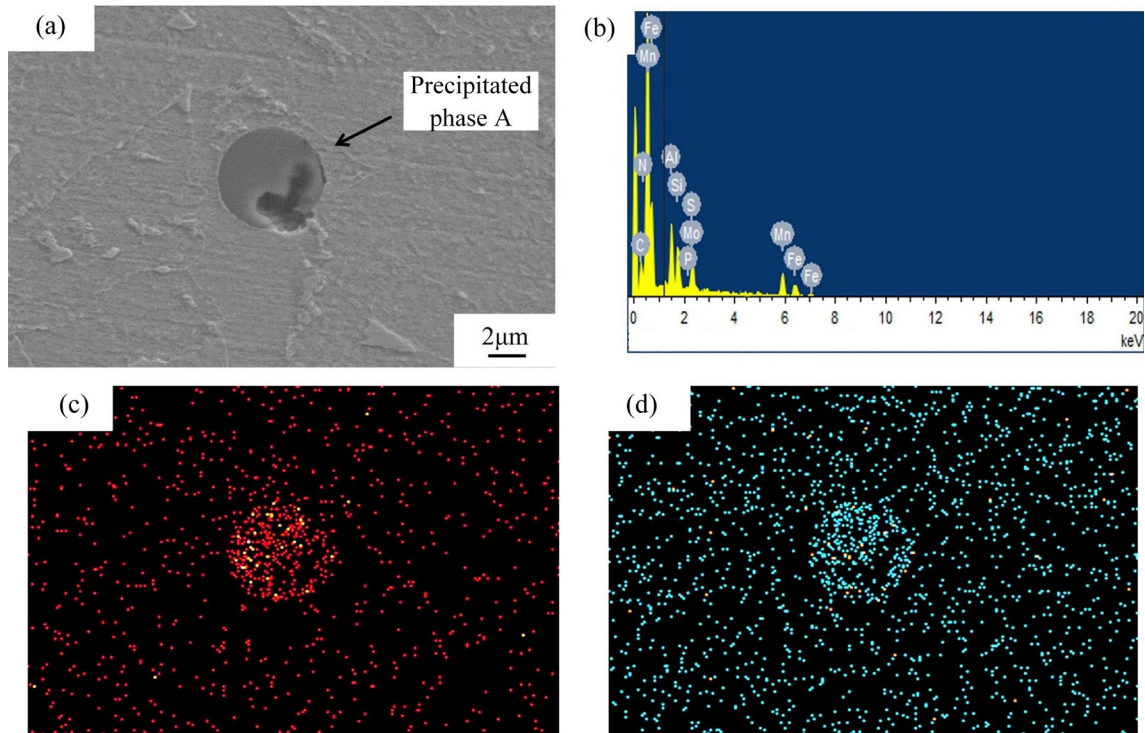


Fig. 9. Precipitated phase and energy spectrum analysis of TFS coarse-grained heat-affected zone: (a) morphology of precipitated phase, (b) result of EDS, (c) distribution of Al, (d) distribution of O

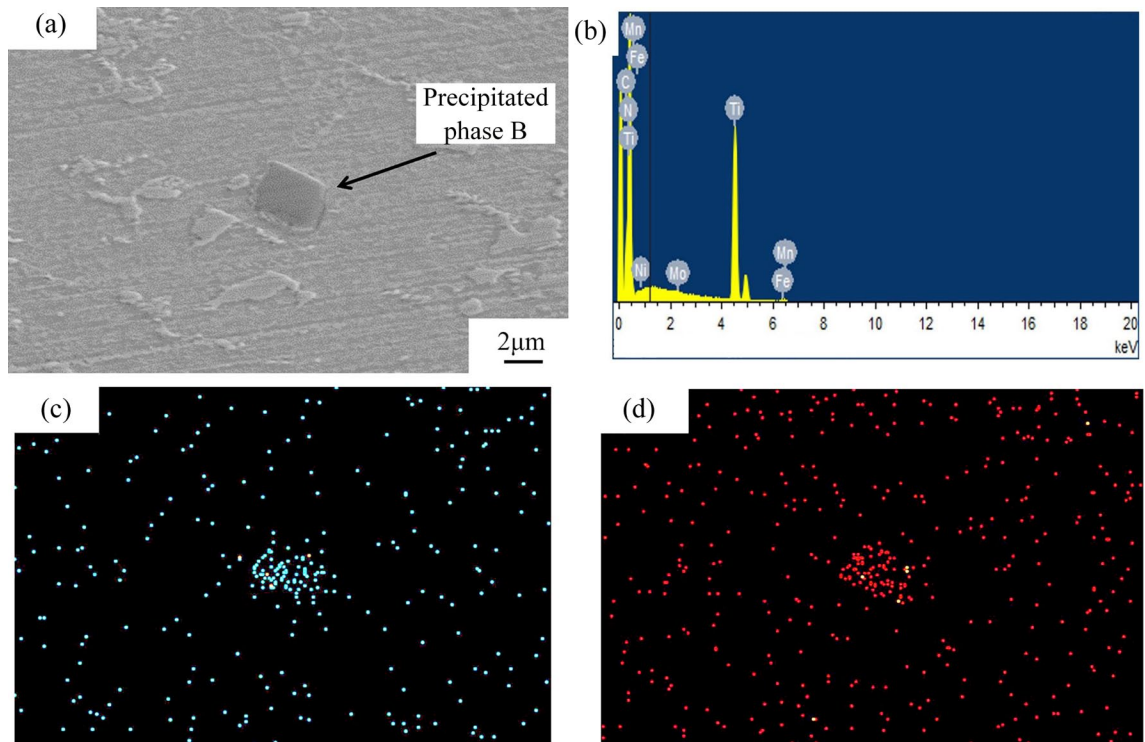


Fig. 10. Precipitated phase and energy spectrum analysis of TCS coarse-grained heat-affected zone: (a) morphology of precipitated phase, (b) result of EDS, (c) distribution of Ti, (d) distribution of N

and N content. The effect of TiN in steel shows that the second phase precipitation pinning can effectively avoid coarsening of austenite grains. The quantity, distribution and size of the second phase precipitates have great influence on the refinement of austenite grains by pinning effect.

Fine grain heat affected zone is also called phase change crystallization zone. The base metal in this area is heated to the temperature of  $1100^{\circ}\text{C}-A_{c3}$ . At this time, pearlite and ferrite will crystallize and transform into austenite, and the formed austenite grain size is smaller than that of the original pearlite



and ferrite, and then decreases with the air cooling temperature, thus forming pearlite and ferrite with uniform distribution and fine size, which is equivalent to the normalized structure after heat treatment, so it is also called normalized area. Because of its fine microstructure, this zone has high plasticity and toughness, and is the best performance zone in the heat affected zone of low carbon steel.

Fig. 11 shows the microstructure of the fine-grained HAZ of TFS. The microstructure of the fine-grained HAZ of the two steels can be seen to be obviously different. From Fig. 11(a) and 11(b), it can be seen that the microstructure of fine grain heat affected zone of TFS is mainly fine grain ferrite structure and some carbides, and the carbide content is relatively high. From Fig. 11 (c) and (d), it can be seen that the microstructure of fine-grained heat affected zone of TCS is fine equiaxed ferrite and a small amount of fine pearlite with uniform distribution. In the fine-grained heat affected zone, carbides cannot bear plastic deformation. If the carbide content increases, the size of the plastic zone at the crack tip will be limited, thus significantly reducing plastic work consumed when micro-cracks occur per unit area. Microcracks can be formed by depolymerization or fracture,

and crack propagation is caused by the mechanism of micropore polymerization and growth, resulting decreasing the toughness of fine grain heat affected zone.

3.2. Effect of Ti on mechanical properties of 12MnNiVR steel joint

Tensile and bending tests of welded joints of TCS and TFS were carried out at room temperature. The results of tensile tests of welded joints at room temperature are shown in TABLE 5. The average tensile strength of welded joints of TFS is 673 MPa, and that of TCS is 676.5 MPa. The tensile strength of welded joints increases slightly after adding Ti, and the fracture position of welded joints occurs at the base metal.

The thickness of 12MnNiVR steel is 21.5 mm. It is impossible to carry out positive bending and back bending tests, so the side bending test method is selected instead, and the defects such as incomplete penetration, cracks, pores and internal stress of welded joints can also be reflected by side bending test. The side bending test results of 12MnNiVR steel welded joints with

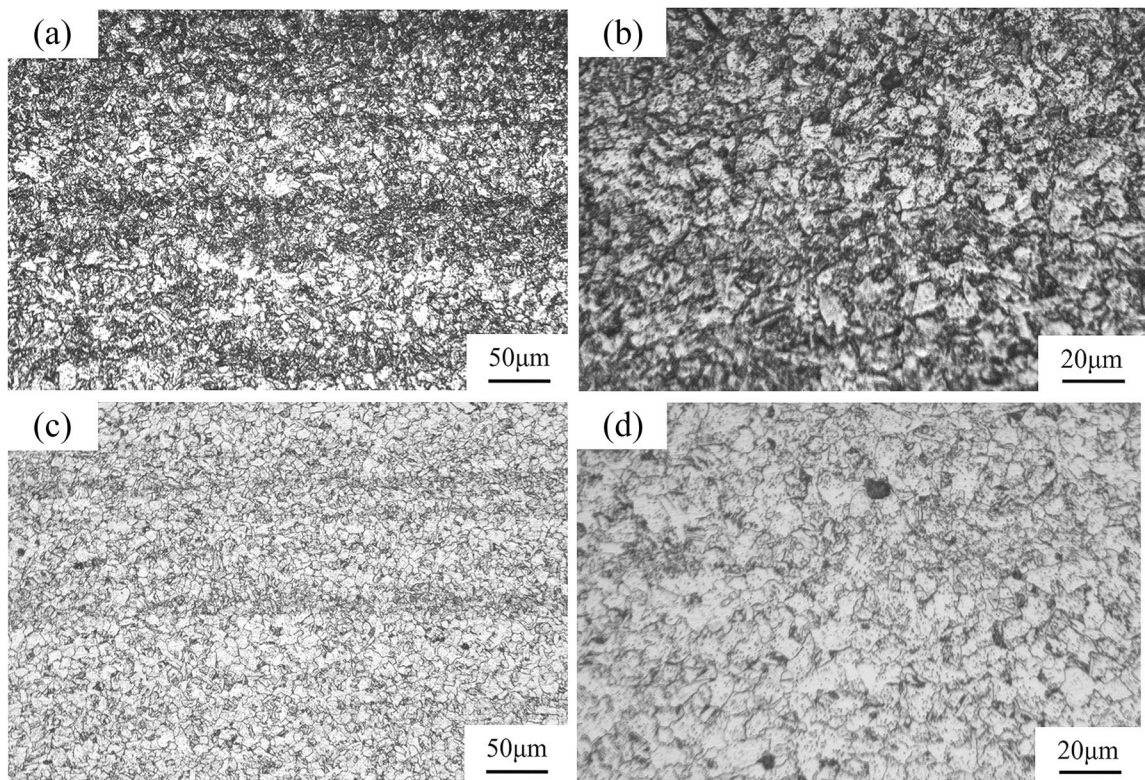


Fig. 11. Microscopic metallography of fine-grained heat-affected zone of 12MnNiVR steel with different compositions: (a) fine-grained HAZ of TFS at low magnification, (b) fine-grained HAZ of TFS at high magnification, (c) fine-grained HAZ of TCS at low magnification, (d) fine-grained HAZ of TCS at high magnification

TABLE 5

Tensile results of welded joints of 12MnNiVR steel with different compositions

12MnNiVR steels	Tensile strength (MPa)	Fracture location
TFS	673 (standard deviation: 1.2)	base metal
TCS	677.5 (standard deviation: 0.6)	base metal



different compositions are shown in TABLE 6. From the surface morphology of side bending samples in Fig. 12, it can be seen that the results of two side bending samples of Ti-containing and TFS welded joints are all qualified and the bending performance is good.

The impact test results of welded joints of TCS and TFS at  $-20^{\circ}\text{C}$  at different zones are shown in TABLE 7 and Fig. 13, with emphasis on the center of weld metal, fusion line and fusion line +2 mm. It can be seen from the chart that the average impact energy at the weld center of TFS is 101.6 J, the average impact energy at the fusion line is 43.6 J, the average impact energy at the fusion line +2 mm is 61.5 J, and the average impact energy at the weld center of TCS is 176.4 J, the average impact energy at the fusion line is 80.1 J, and the average impact

energy at the fusion line + 2 mm is 163.1 J. The impact toughness of 12MnNiVR steel welded joint is obviously improved by adding Ti. The impact toughness at the weld center is increased by 73.6%, the fusion line is increased by 83.7%, and the fusion line +2 mm is increased by 165.2%. Only the impact energy of welded joints of TCS meets the standard. It can be seen from Fig. 13 that the impact energy of welded joints of TCS is higher than that of welded joints of TFS, and the impact absorption energy in each region is greatly affected by the microstructure in this region, and there are differences in precipitates in grains, which leads to differences in impact absorption energy.

There are a lot of carbon-free bainite in the heat affected zone of TCS. The bainite transformation is carried out at a lower temperature and a finer size of bainite ferrite slats is obtained.

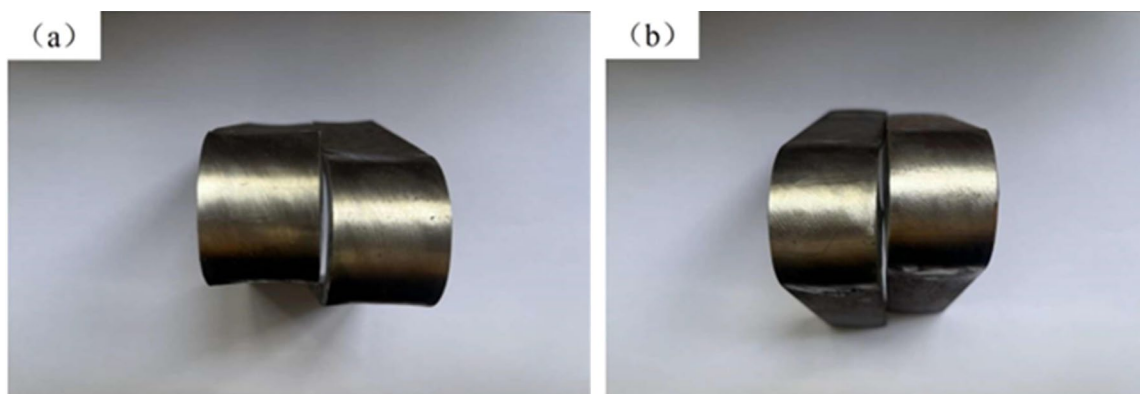


Fig. 12. Surface morphology of side bending specimens of 12MnNiVR steel welded joints with different compositions: (a) TFS, (b) TCS

TABLE 6

Side bending results of welded joints of 12MnNiVR steels with different compositions

12MnNiVR steels	Thickness of specimen (mm)	Bending angle ( $^{\circ}$ )	Testing Result
TFS	10	180	No crack
	10	180	No crack
TCS	10	180	No crack
	10	180	No crack

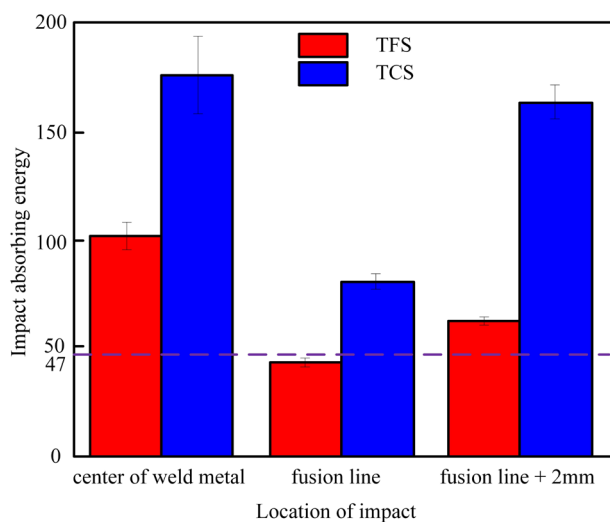


Fig. 13. Impact properties of different regions of 12MnNiVR steel welded joints with different compositions

However, the mean path of dislocation free sliding is limited by the finer bainite ferrite slats, which is conducive to the improvement of the structure strength. In addition, there is no cementite in carbon-free bainite, which improves the resistance of the tissue to the formation of dimple and cleavage fracture, and improves the fracture property of the material. The thin film residual austenite distributed between the bainitic ferrite slats can passivate the crack tip, hinder the crack propagation to a certain extent, and also contribute to the improvement of toughness. A small amount of slender M-A component in HAZ also plays a role in improving toughness. When a small massive M-A island is encountered in the process of crack growth, the direction of crack growth changes and the further development of crack is delayed. When the crack source is generated in the tiny massive M-A island, there is no crack growth, and a secondary crack of micropore aggregation is formed, which alleviates the stress concentration through plastic deformation

and absorbs the impact energy. Therefore, TCS has better impact performance than TFS.

Fracture surface is the fracture of specimen in the process of impact test, and then forms a matching surface. Fracture formation includes the whole failure process from crack initiation, propagation to fracture. In the impact test, when the pendulum drops to impact the specimen, the plastic deformation begins to occur at the notch under the action of load impact force, and micro-cracks initiate at the root of the notch. The crack source slowly and smoothly expands from the notch, forming a fiber area with obvious directivity, undulating gully shape and no metallic luster. The formation of fiber region indicates that the specimen has good plasticity. When the crack propagates to the edge of the fibrous region, the rapid instability propagation occurs, and a radial region with rough undulating white crystal is formed in the center of the fracture surface. After that, the crack propagates into the low stress zone. At this time, the remaining section of the specimen is in a state of plane stress, and the plastic deformation is less constrained. Shear stress will cause fracture, and finally form a smooth shear lip area, which is gray.

Fig. 14 shows the macroscopic morphology of impact fracture of welded joints of TCS and TFS. It can be seen from Figure 14 that the fiber zone, radiation zone and shear lip of impact fracture at the center of weld of TFS are evenly distributed and obvious. The impact fracture at fusion line and fusion line +2 mm is mainly radial zone, which leads to the decrease of plastic deformation. However, in Fig. 14, the impact fracture surface at the center of the weld of TCS has a significant uneven dark gray fibrous morphology, and smooth and dark gray shear lips appear around the edge of the sample; At the fusion line, there is more than half of the radiation area of the impact fracture surface, which is rough and undulating white crystal, and the fiber area and shear lip are not obvious; However, the fiber area on the impact fracture surface at the fusion line +2 mm is relatively uniform and the area is large, which indicates

that the crack propagates slowly and evenly in this area, which makes the deposited metal show high toughness. The greater the plastic deformation of the specimen during impact, the greater the lateral expansion coefficient and the greater the impact energy; For materials with low impact toughness, the proportion of fiber zone is small, the radiation zone is the main part, and the lateral expansion value of fracture surface is low. Therefore, the impact energy of welded joints of TCS is greater than that of welded joints of TFS.

The impact fracture of welded joints of two kinds of steels was analyzed by scanning electron microscope, and the micro-morphology of impact fracture is shown in Fig. 15. The number of dimples in the fracture surface of TFS is small and shallow, which indicates that the crack mainly propagates along a single direction during the fracture process, resulting in small plastic deformation, so the absorption energy is less and the impact absorption work is lower, which is consistent with the test results; Tear edges, cleavage steps and cleavage facets can be clearly seen in the fracture morphology at fusion line and fusion line +2 mm, and river patterns can be observed on cleavage facets. However, the fracture morphology of TCS is dimple-shaped at the center of weld, which has obvious equiaxed dimple characteristics; The fracture morphology at the fusion line is mainly characterized by quasi-cleavage morphology, and there are a few dimples; Fracture morphology at +2 mm of fusion line shows that there are many dimples with deep depth and dense arrangement, and there are many small dimples around the big dimples, which shows that the metal has great plastic deformation during fracture, and absorbs more energy and impact energy during fracture.

The microhardness results of welded joints made of 12MnNiVR steel with varying compositions are displayed in Fig. 16. Compared to the average microhardness in the TFS weld metal (204 HV<sub>10</sub>), the average microhardness in TCS weld metal was about 221 HV<sub>10</sub>, indicating an 8.3% increase in microhardness with adding Ti. The maximum microhardness

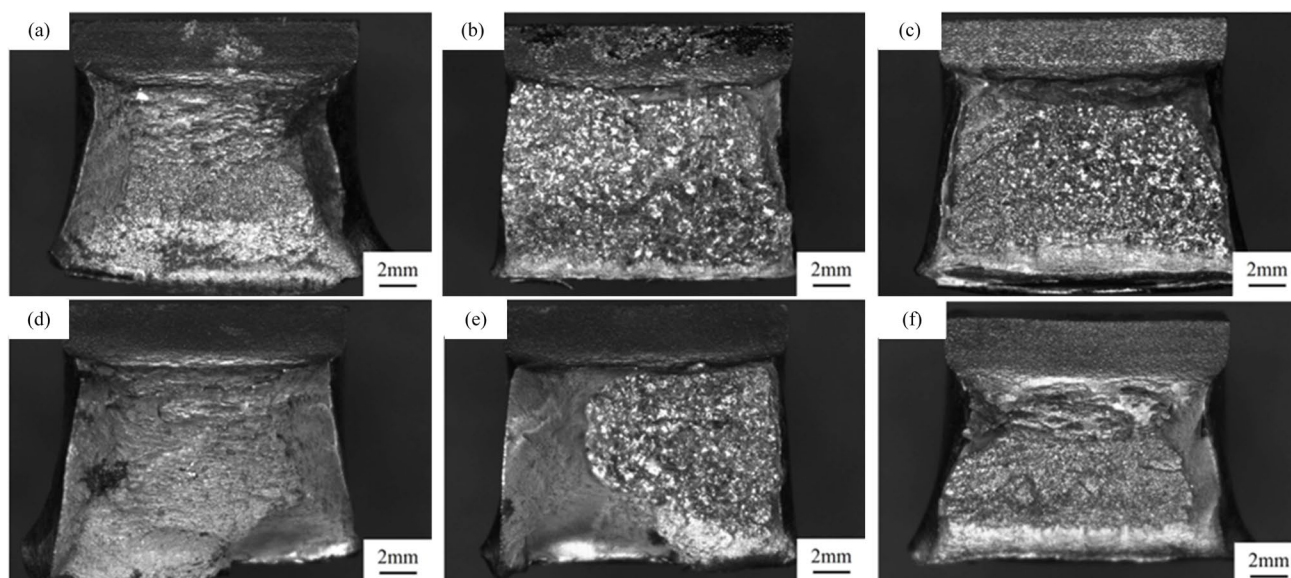


Fig. 14. Fracture surface of welded joints of 12MnNiVR steel: (a) the center of weld metal of TFS, (b) fusion line of TFS, (c) fusion line +2 mm of TFS, (d) the center of weld metal of TCS, (e) fusion line of TCS, (f) fusion line +2 mm of TCS



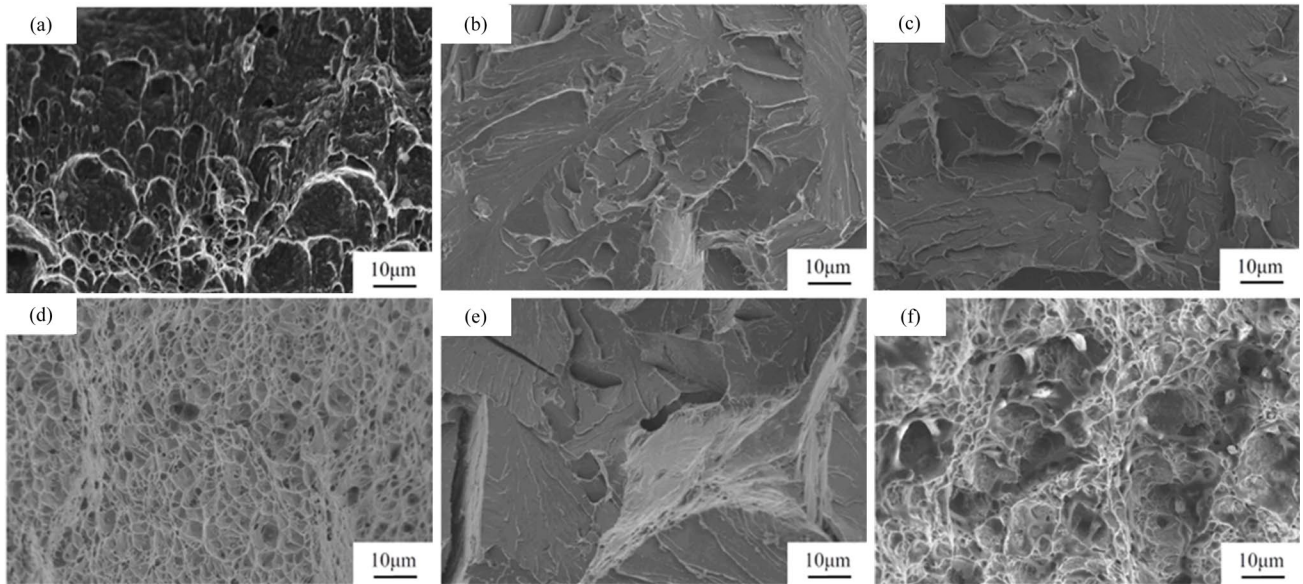


Fig. 15. Fracture morphology of welded joints of 12MnNiVR steel: (a) the center of weld metal of TFS, (b) fusion line of TFS, (c) fusion line +2 mm of TFS, (d) the center of weld metal of TCS, (e) fusion line of TCS, (f) fusion line +2 mm of TCS

in the heat affected zone of TFS is 213 HV<sub>10</sub> and the minimum microhardness is 170 HV<sub>10</sub>. The maximum microhardness in the heat affected zone of TFS is 212 HV<sub>10</sub> and the minimum microhardness is 178 HV<sub>10</sub>. It is indicated that Ti has little effect on the maximum value of microhardness in the heat affected zone.

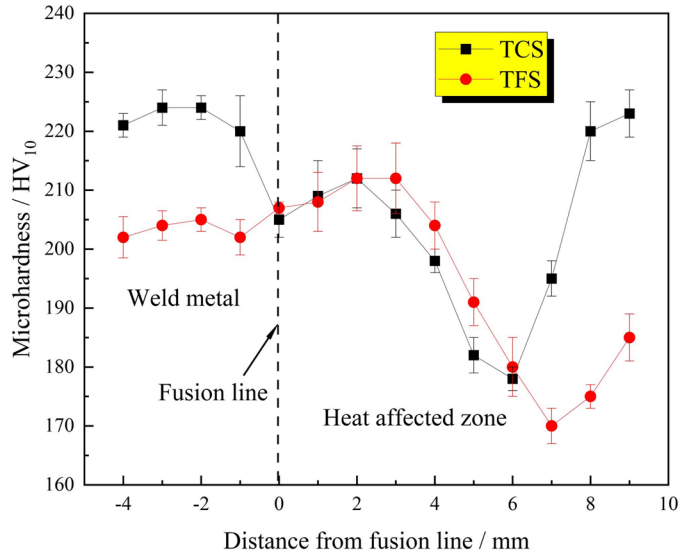


Fig. 16. The distribution of microhardness of joints

#### 4. Conclusions

The microstructure, precipitates and precipitated phase of welded joints of TCS and TFS under 100 kJ/cm heat input were analyzed by OM, SEM, EDS. The difference of mechanical properties between welded joints of TCS and TFS is analyzed. Conclusions can be obtained as follows.

- (1) The microstructure of TFS weld metals is mainly coarse acicular and massive proeutectoid ferrite, coarse acicular

ferrite Widmanstatten structure and granular bainite. The microstructure of TCS weld metal is mainly granular bainite and acicular ferrite.

- (2) The microstructure of the partial melted zone of TFS is Widmanstatten side lath ferrite and upper bainite. The microstructure of partial melted zone of TCS is fine granular bainite and side lath ferrite.
- (3) The microstructure of coarse-grained heat affected zone of TFS is granular bainite, upper bainite, massive ferrite and lath bainite; The microstructure of coarse-grained heat affected zone of TCS is granular bainite, acicular and lath proeutectoid ferrite, acicular ferrite with different thickness and a large number of carbon-free bainite.
- (4) The microstructure of fine-grained heat affected zone of TFS is fine granular ferrite and a little carbide; The microstructure of fine-grained heat affected zone of TCS is fine equiaxed ferrite and a small amount of fine pearlite with uniform distribution.
- (5) Ti has little effect on the tensile and flexural properties of welded joints, but it can improve the impact toughness of welded joints, from 101.6 J to 176.4 J at the center of weld, from 43.6 J to 80.1 J at the fusion line, from 61.5 J to 163.1 J at the fusion line + 2 mm, increasing by 73.6%, 83.7%, 165.2%, and the content of Ni and Ti in the dimples of impact fracture surface is high.

#### Acknowledgement

This work is supported by the Natural Science Foundation of the Higher Education Institutions of Jiangsu Province (Grant No. 24KJA460002) and Natural Science Foundation of Jiangsu Province (Grant No. BK20210890 & BK20210873).

## REFERENCE

- [1] G. Wu, J. Luo, L. Li, Y. Long, S. Zhang, Y. Wang, Y. Zhang, S. Xie, *Metals* **12**, 1502 (2022).
- [2] R. Cao, Z. Yang, J. Li, X. Liang, W. Lei, J. Zhang, J. Chen, *Journal of Materials Engineering and Performance* **29**, 7063-7072 (2020).
- [3] X. Ouyang, X. Hu, C. Liu, C. Wang, C. Jia, M. Xing, *Journal of Physics: Conference Series* **2539**, 012078 (2023).
- [4] O. Xin, H. Xinming, S. Diandong, W. Chu, W. Yong, X. Mengnan, *Journal of Physics: Conference Series* **2011**, 012018 (2021).
- [5] J. Fu, Q. Tao, X. Yang, B. Nenchev, M. Li, B. Tao, H. Dong, *Materials* **15**, 2215 (2022).
- [6] T. Kakizaki, S. Koga, H. Yamamoto, Y. Mikami, K. Ito, K. Yamazaki, S. Sasakura, H. Watanabe, *Welding in the World* **66**, 313-324 (2022).
- [7] K. Seo, H. Ryoo, H.J. Kim, C.-G. Park, C. Lee, *Welding in the World* **64**, 457-465 (2020).
- [8] F. Liu, C. Tao, Z. Dong, K. Jiang, S. Zhou, Z. Zhang, C. Shen, *Materials Today Communications* **29**, 102786 (2021).
- [9] Y. Chen, C. Fang, T. Zhang, Q. Li, Q. Hong, L. Hua, *Journal of Manufacturing Processes* **55**, 96-102 (2020).
- [10] T. Li, D. Zhou, Y. Yan, S. Zhang, J. Liu, *Materials Science and Engineering: A* **796**, 139929 (2020).
- [11] J. Li, B. Schneiderman, S. Song, S.M. Gilbert, A. Vivek, Z. Yu, P. Dong, G.S. Daehn, *The International Journal of Advanced Manufacturing Technology* **108**, 1447-1461 (2020).
- [12] K. Liu, P. Yu, S. Kou, *Welding Journal* **99**, (2020).
- [13] Z. Yuan, Y. He, F. Xie, X. Kang, *Intermetallics* **152**, 107767 (2023).
- [14] X. Gao, W. Li, Y. Fan, J. Zou, K. Yan, J. Tang, K. Liu, *Metallic Materials/Kovové Materiály* **61**, (2023).
- [15] Q. Tan, K. Liu, J. Li, S. Geng, L. Sun, V. Skuratov, *Journal of Alloys and Compounds* **1001**, 175164 (2024).
- [16] L. Wang, K. Liu, J. Li, Z. Chen, J. Wang, A. Okulov, *Vacuum* **219**, 112709 (2024).
- [17] A. Rong, L. Zhao, C. Pan, Z.-L. Tian, *Journal of Iron and Steel Research, International* **22**, 431-437 (2015).
- [18] H.H. Wang, G.Q. Li, X.L. Wan, H.H. Wang, K.C. Nune, Y. Li, K.M. Wu, *Science and Technology of Welding and Joining* **22**, 133-142 (2017).
- [19] B.Z. Li, C.S. Li, X. Jin, J. Zhang, *Journal of Iron and Steel Research International* **26**, 1340-1349 (2019).
- [20] E. Erişir, O.G. Bilir, Y.E. Sözer, Ö. Ararat, K. Davut, *Materials Science and Technology* **39**, 105-116 (2023).
- [21] P. Mohseni, J.K. Solberg, ØM. Karlsen, O.M. Akselsen, E. Østby, *Metallurgical and Materials Transactions A* **45**, 384-394 (2014).